



Source characterization for an explosion during the 2009 eruption of Redoubt Volcano from very-long-period seismic waves

Matthew M. Haney ^{a,*}, Bernard A. Chouet ^b, Phillip B. Dawson ^b, John A. Power ^a

^a Alaska Volcano Observatory, U.S. Geological Survey, Anchorage, Alaska, USA

^b U.S. Geological Survey, Menlo Park, California, USA

ARTICLE INFO

Article history:

Received 7 June 2011

Accepted 12 April 2012

Available online 1 May 2012

Keywords:

Explosive eruptions

Seismology

Volcanism

Very-long-period seismicity

ABSTRACT

The 2009 eruption of Redoubt produced several very-long-period (VLP) signals associated with explosions. We invert for the source location and mechanism of an explosion at Redoubt volcano using waveform methods applied to broadband recordings. Such characterization of the source carries information on the geometry of the conduit and the physics of the explosion process. Inversions are carried out assuming the volcanic source can be modeled as a point source, with mechanisms described by a) a set of 3 orthogonal forces, b) a moment tensor consisting of force couples, and c) both forces and moment tensor components. We find that the source of the VLP seismic waves during the explosion is well-described by either a combined moment/force source located northeast of the crater and at an elevation of 1.6 km ASL or a moment source at an elevation of 800 m to the southwest of the crater. The moment tensors for the solutions with moment and force and moment-only share similar characteristics. The source time functions for both moment tensors begin with inflation (pressurization) and execute two cycles of deflation-reinflation (depressurization-repressurization). Although the moment/force source provides a better fit to the data, we find that owing to the limited coverage of the broadband stations at Redoubt the moment-only source is the more robust and reliable solution. Based on the moment-only solution, we estimate a volume change of 19,000 m³ and a pressure change of 7 MPa in a dominant sill and an out-of-phase volume change of 5000 m³ and pressure change of 1.8 MPa in a subdominant dike at the source location. These results shed new light on the magmatic plumbing system beneath Redoubt and complement previous studies on Vulcanian explosions at other volcanoes.

Published by Elsevier B.V.

1. Introduction

Very-long-period (VLP) seismic radiation, within the frequency band from 0.01 Hz to 0.5 Hz, is commonly observed with volcanic activity. By virtue of the fact that seismic waves suffer little path distortion in the VLP band at volcanoes (Cesca et al., 2008), VLP events offer a window through which important source processes can be observed (Chouet, 2009). The ability to record VLP events in the near-field is a recent development in volcano seismology, but in the decade since its discovery such seismicity has been observed worldwide. Distinct VLP events, with durations less than 200 s, have been observed at many volcanoes, including Kilauea (Ohminato et al., 1998; Chouet et al., 2010; Dawson et al., 2010), Stromboli (Chouet et al., 2003; Auger et al., 2006; Chouet et al., 2008), Popocatepetl (Arciniega-Ceballos et al., 1999; Chouet et al., 2005; Arciniega-Ceballos et al., 2008), Asama (Ohminato et al., 2006), Iwate (Nishimura et al., 2000), Miyake Island (Kumagai et al., 2001), Erebus (Aster et al., 2008), Fuego (Lyons &

Waite, 2011), Mt. St. Helens (Waite et al., 2008), and Augustine (Dawson et al., 2011). Long-duration VLP seismicity, or VLP tremor, has been observed at Stromboli (DeLauro et al., 2005), Okmok (Haney, 2010), and Kilauea (Dawson et al., 2010). VLP signals were also observed to accompany explosions during the 2009 eruption of Redoubt Volcano, Alaska. Quantitative analysis of these VLP signals contributes further insights to what is already known about the volcano's shallow magmatic system.

Redoubt Volcano is a composite volcano on the western side of Cook Inlet, Alaska, that erupted over 4 months in 2009, beginning on March 22 and ending when dome growth ceased in July. The volcano rises to a peak elevation of 3.108 km and is covered by several glaciers. Previous eruptive periods at Redoubt occurred in 1966–68 and 1989–90 and were marked by episodes of dome building and destruction. The seismicity observed during the 1989–90 eruption led to a fundamental advance in the understanding of different types of volcanic seismicity and resulted in a widely-used classification of volcanic earthquakes as volcano-tectonic (VT), long-period (LP), and hybrid types. The scientific results of the 1989–90 sequence have been described in a previous special issue on the 1989–90 Redoubt eruption (Chouet et al., 1994; Lahr et al., 1994; Power et al., 1994).

* Corresponding author.

E-mail address: mhaney@usgs.gov (M.M. Haney).

We describe the source mechanism of VLP signals associated with an explosion at Redoubt during the 2009 eruption. Among several possible instances of VLP seismicity, we select a single explosion with a short duration (<200 s) signal for further analysis. We first discuss the broadband network installed at Redoubt during the 2009 eruption and review the main features of the 2009 eruption seismicity. Following this broad overview, we focus our attention on the VLP signals from one explosion and analyze the low-frequency particle motions observed on the broadband network. An inherent assumption in the waveform inversion method we present is that the source can be described by a set of moments and forces acting at one point in the subsurface. The explosion we select has been chosen since it has a short duration and compact waveform. Such an explosive event is more likely to be the result of a source acting at a single point in the subsurface than explosions with longer signal durations and more complex waveforms. We find best-fitting source models based on combinations of forces and moments by searching over appropriate volumes within the Redoubt edifice. Two different source models in particular provide a reasonable fit to the instrument-corrected displacement seismograms. We argue that, based on the limited number of broadband channels at Redoubt (13), the source model with only moments and no forces is the most robust solution. These findings regarding the resolving power of source mechanism inversion with limited observational data agree with previous work on VLP signals associated with an explosion during the 2006 eruption of Augustine volcano (Dawson et al., 2011). The magnitude of the inverted moment tensor at Redoubt is nearly the same as observed at Augustine and the source time function bears a strong resemblance to VLP sources imaged at other volcanoes during explosions (Chouet et al., 2005; Dawson et al., 2011).

2. Broadband data and VLP signals at Redoubt

VLP signals were observed to accompany explosions during the 2009 eruption of Redoubt. Similar signals were not previously detected at Redoubt during the 1989–90 eruption due to the lack of broadband seismic coverage at that time. Other novel seismic phenomena observed during the 2009 eruption consisted of rapid, ascending spectral gliding immediately prior to some explosions dubbed volcanic “screams” (Hotovec et al., 2013) and deep long-period (DLP) events in the months prior to the eruption (Power et al., 2013). All three of these phenomena may have occurred during the 1989–90 eruption; however, instrumentation and methods at that time were not advanced enough to detect them. The observation of these seismic phenomena during the 2009 eruption offers a more complete picture of the Redoubt magmatic system than could be inferred from the seismicity during the 1989–90 eruption.

In the days leading up to the initial explosions on March 22, scientists from the Alaska Volcano Observatory, a partnership between the University of Alaska–Fairbanks Geophysical Institute, the Alaska Division of Geological and Geophysical Surveys, and the U.S. Geological Survey, placed 4 broadband seismometers on the flanks of the Redoubt edifice. The locations of these temporary broadband stations are shown in Fig. 1. The stations varied in elevation from 1.32 to 1.85 km and in range to the 1989–90 dome from 2.9 to 4.4 km laterally. The instruments were Guralp 6-TD broadband seismometers (0.02–30 s) that recorded three-component data on site at 50 samples-per-second (sps) from March 21 until the early part of June. In addition to these temporary installations, a single broadband station in the permanent monitoring network was in operation on the Redoubt edifice, station RDWB as seen in Fig. 1. The permanent monitoring network consisted of several other short period instruments — we plot two of these stations, DFR and RDE, in Fig. 1 and show data from these stations in subsequent figures. Note that station DFR consisted of a co-located short period seismometer and infrasound microphone. The temporary broadband station RD01 was co-located with a three-component short period station REF, which we also show data from in subsequent figures. The 5 three-

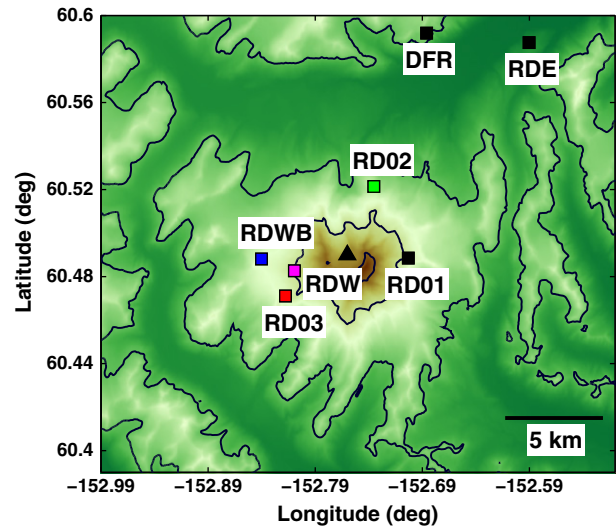


Fig. 1. Map of the 4 broadband seismometers temporarily deployed at Redoubt Volcano from March through June 2009. Contours are given at 3000, 6000, and 9000 ft ASL, according to the convention from Chouet et al. (1994) and Lahr et al. (1994). One broadband (RDWB) was in operation on the Redoubt edifice within the permanent network, bringing the total number of broadband sensors to 5. Lateral distance from the 1989 to 90 dome ranged from as close as 2.9 km (RDW) to 4.4 km (RDWB). Elevations ranged from 1.32 km (RD02) to 1.85 km (RDW). Short period stations DFR and RDE, which are discussed in the caption of Fig. 2, are located on the northern side of the Drift River valley. Short period station REF is co-located with RD01.

component broadband stations on the Redoubt edifice offered as many as 15 components of VLP recordings; however, the north–south components of RD02 and RDW were not functioning properly during the temporary deployment. This limits the number of available components to 13, one less than the number of components (14) used for source mechanism inversions at Augustine Volcano (Dawson et al., 2011). This is an important point that we will return to in this paper, since the main conclusion of the study by Dawson et al. (2011) concerned the resolution power of source mechanism inversions when using a limited amount of broadband data.

Shown in Figs. 2 and 3 are the first 18 explosive events during the Redoubt 2009 eruption, as identified by scientists monitoring volcanic activity during the eruption at the Alaska Volcano Observatory. Additional small events have been identified in retrospect but are not included in Figs. 2 and 3. Two significant events are also not included in the figures: the dome-destroying explosion on April 4, 2009 (event #19) and an LP earthquake swarm in early May that was associated with a small ash emission from the dome. As seen in Figs. 2 and 3, the seismic and infrasonic radiation from the early explosive events (#1–9) varied dramatically compared to the later events (#10–18) which became more consistent and short in duration. Figs. 2 and 3 show that several events produced measurable VLP energy: this is evident in the low-pass filtered seismograms from the broadband instrument RDWB (the second data stream from the top in each panel). We selected the compact VLP waveform from event #12 for further analysis. This event likely occurred at a time when a dome did not exist within the crater, such as the dome that was destroyed by the April 4 event. The explosion from event #12 generated an ash-rich volcanic plume that reached an altitude of approximately 12 km (40,000 ft) ASL. Event #12 shares a similar VLP waveform with events #11 and #13 and infrasound signals in the far-field show similar waveforms for these events (Fee et al., 2013). Event #12 is also interesting since it is one of the subset of events that exhibited volcanic “screams” immediately prior to the explosion (Hotovec et al., 2013).

To the raw broadband recordings, we apply a causal instrument correction over the period band 10–33 s to allow the analysis of the VLP signals in physical units. The choice of the cutoffs at 10 s and

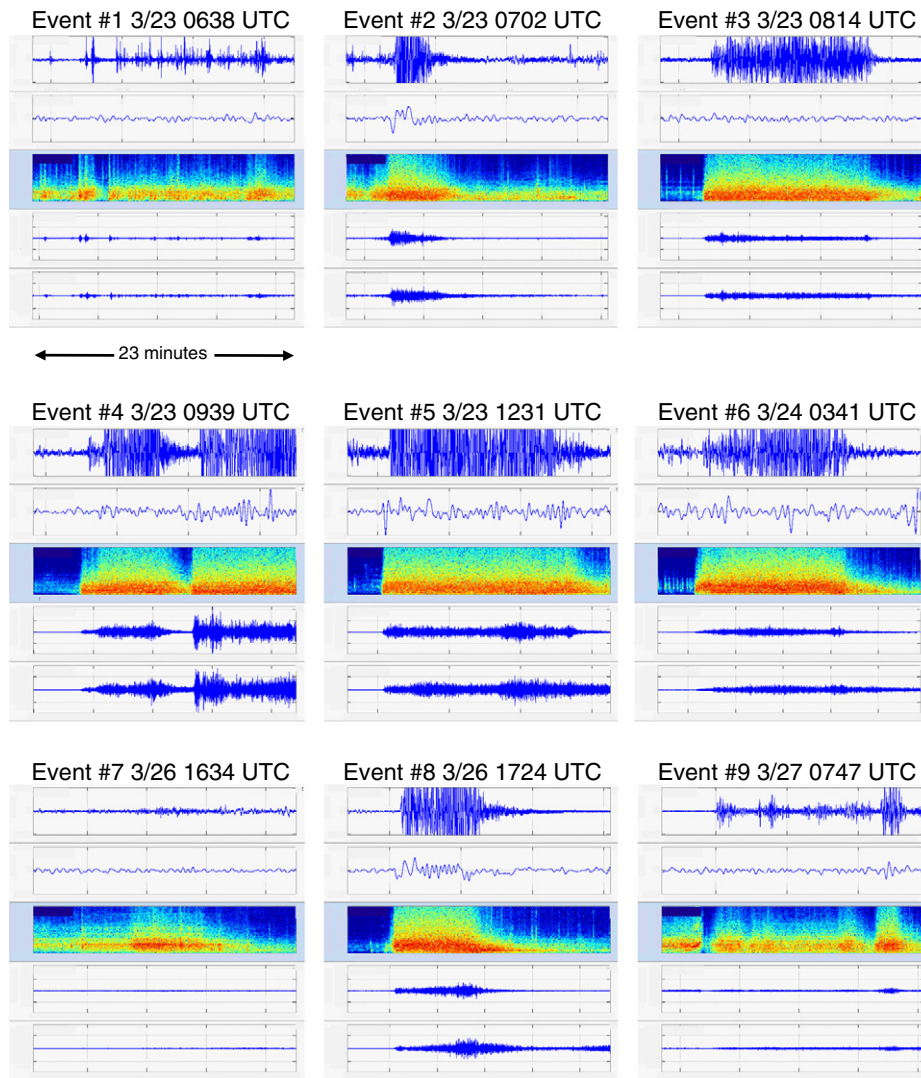


Fig. 2. The first 9 explosive events of the 2009 Redoubt eruption. Shown for each event are 5 data streams consisting of (top to bottom): high-gain pressure sensor DFR, low-pass filtered (<0.05 Hz) broadband RDWBz, spectrogram of summit station REFz from 0 to 25 Hz, unfiltered broadband RDWBz, and short-period station RDE. For each event, 23 min of data are plotted. Lahars are evident in the extended tails of RDE relative to the unfiltered RDWBz for events #5, #6, and #8. Compact VLP waveforms exist for events #2, #5, and #8.

33 s period are intended to avoid persistent microseismic noise for periods less than 10 s and to remain within the passband of the broadband instruments (<30 s). The method for our causal instrument correction has been described by Haney et al. (in press) and involves the use of the bilinear transform and oversampling. Haney et al. (in press) demonstrated the accuracy and stability of this instrument correction by comparing data recorded on a co-located short period and broadband seismometer at Mt. Spurr Volcano, Alaska. The instrument correction yields the displacement seismogram at RD03 in Fig. 4 for event #12. The maximum displacement at station RD03 is observed to be in excess of $50\ \mu\text{m}$ at a distance of 4 km from the crater. The first motion on the vertical component is up and the horizontal first motion is toward the southwest. The VLP signal has a remarkably clear onset on the east–west component and has a duration of 1 to 2 min. With RD03 located west of the crater, the dominantly east–west motion demonstrates the overall radial character of the VLP signals. We explore this further in the next section by analyzing the three-component particle motions in the VLP band from 10 to 33 s. In Fig. 5, we plot the amplitude spectrum of the vertical component of station RDWB both in terms of displacement (top) and particle velocity (bottom). The displacement spectrum, with a peak frequency of 0.04 Hz (25 s peak period), provides further support for the emphasis on the VLP signals in the source inversion.

The particle velocity spectrum, on the other hand, shows that the VLP signals do not stand out in a raw seismogram, which is proportional to particle velocity. The dominant periods within the particle velocity spectrum exist close to 2 s period.

3. VLP particle motions

Initial indications for the location of the VLP signals can be gained through the analysis of particle motions on the 5 broadband stations. This is an important processing step prior to source mechanism inversion since the source optimization process requires a grid search within the volcanic interior for the source location. By studying the particle motions, the subsurface volume containing the source can be better constrained, leading to a more refined and efficient grid search. This is possible since the particle motions of VLP events are often highly rectilinear and directed radially towards and away from the source (Almendros & Chouet, 2003).

In Fig. 6 we plot the particle motions for event #12 in map view. The particle motions have been exaggerated in order to facilitate visualization; however, this exaggeration has been done such that the relative amplitudes between stations are preserved. Also shown as circles and boxes are source locations and grid search volumes that we describe in a later section. Notice that no particle motions are

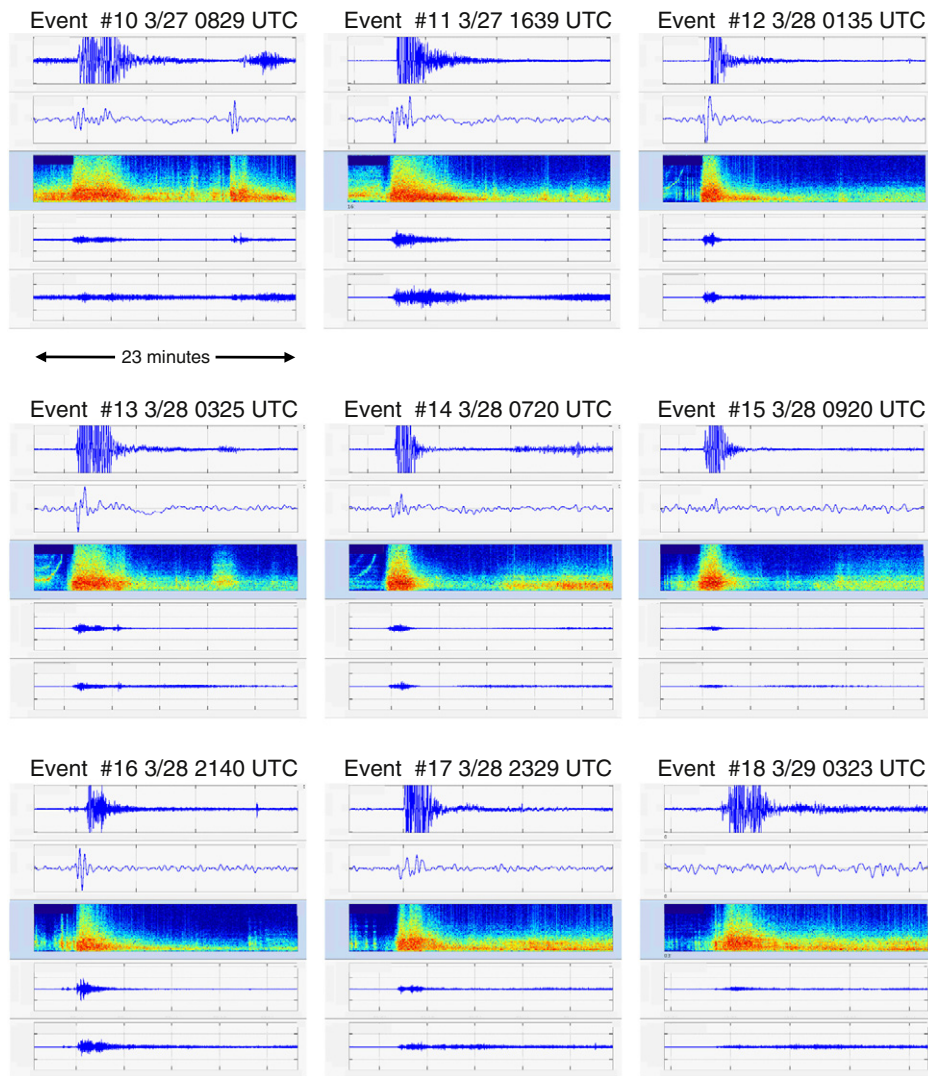


Fig. 3. Explosive events 10–18 of the 2009 Redoubt eruption. Shown for each event are 5 data streams as described in the caption for Fig. 2. For each event, 23 min of data are plotted. A lahar is evident in the extended tail of RDE relative to the unfiltered RDWBz for event #11. Compact VLP waveforms exist for events #10–#14 and #16–#17. Spectral gliding appears in events #11–#14.

plotted at stations RD02 and RDW. As mentioned earlier, these two stations did not have functioning north–south components, hence, the particle motions cannot be projected into the horizontal plane at

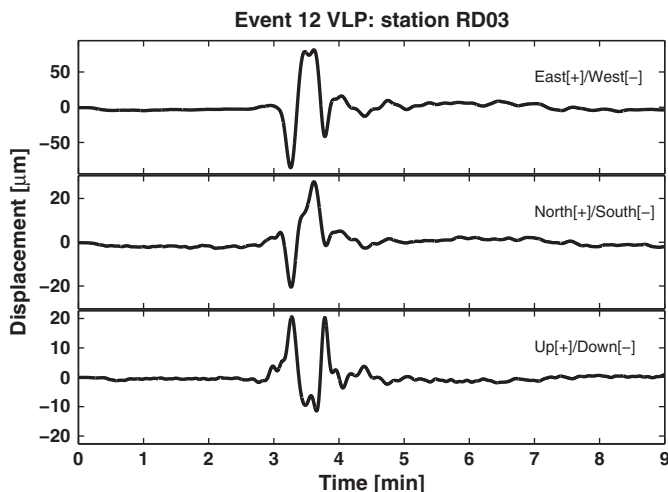


Fig. 4. Instrument-corrected VLP waveforms from the three-component broadband station RD03 for event #12.

these receivers. For stations RD01 and RD03, the particle motions point roughly in a radial pattern from the crater. This property of the VLP signals is in agreement with observations made at many other volcanoes (Almendros & Chouet, 2003; Chouet et al., 2003, 2005; Lyons & Waite, 2011) and is indicative of the explosive character of the event. As plotted in Fig. 6, station RDWB also shows an approximately radial particle motion. However, note that we have switched the horizontal components for plotting RDWB in Fig. 6. Without the switching of the horizontal components, RDWB would show a tangential particle motion relative to the crater location. Such a tangential particle motion for explosive VLP signals is highly unusual (Chouet et al., 2005; Lyons & Waite, 2011). Moreover, the east–west components of the stations closest to RDWB, RD03 and RDW, closely match the raw north–south component of station RDWB in both waveform and amplitude. We return to this point in a later section of this paper and further illustrate the match between the east–west components of RD03 and RDW and the north–south component of RDWB. Based on this close match and the fact that the stations RDWB, RD03, and RDW sit relatively close to one another on the western flank of Redoubt, we have concluded that the horizontal components of RDWB are in fact switched and proceed to plot RDWB taking this switch into account. Although we have concluded that the horizontal components are switched based on the VLP signal from the Redoubt explosion in late March, we have been unable to verify this switching of components for teleseisms recorded on

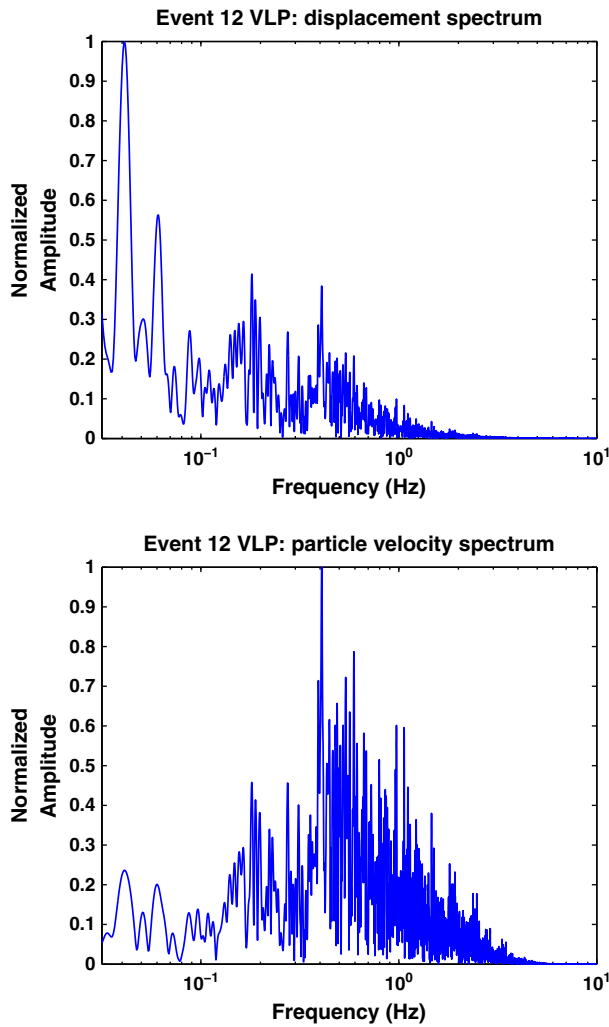


Fig. 5. Displacement (top) and particle velocity (bottom) spectra from the vertical component of station RDWB for event #12. The VLP frequency band utilized in the inversions, from 0.03 to 0.1 Hz (10–33 s period), dominates the displacement seismogram, with a dominant frequency of about 0.04 Hz (25 s period). The VLP frequencies do not, however, dominate raw seismograms which are proportional to particle velocity.

April 1 and 7. Thus, the cause of the component switch is unclear. A possible factor is that, of the 5 broadband stations at Redoubt, only RDWB telemetered data in real-time. The other 4 broadband stations recorded data on site.

Since the north–south components are lacking on 2 of the 5 stations, we can maximize the number of available stations by looking at particle motions projected into the east–west vertical plane. In Fig. 7, we show the projection onto the east–west vertical plane with particle motions again exaggerated for visualization. The vertical exaggeration in Fig. 7 is a factor of 2. As in Fig. 6, source locations and grid search volumes that we describe in a later section are shown as circles in boxes. The particle motions point radially towards and away from a source region below the crater at roughly 1 km ASL. These observations provide strong evidence that the source of event #12 originated at an elevation of approximately 1 km ASL and more or less beneath the crater. We utilize this initial indication for the source location to guide the selection of subsurface volumes for our grid search for best-fit source.

4. Source mechanism inversion

We seek to invert the VLP signals observed during event #12 at Redoubt for the location and precise mechanism of the explosion within the volcano. The method we employ has been applied to many

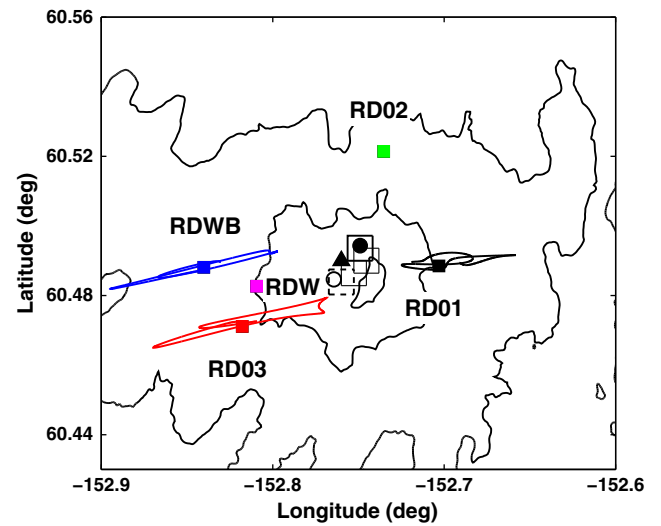


Fig. 6. Map of the 5 summit broadband sensors plotted along with exaggerated particle motions. Stations RDW and RD02 had inoperative north–south components, and are not represented in this plot. Contours are given as in Fig. 1. The crater is shown as a black triangle and the VLP particle motions show a more or less radial pattern away from the crater. Also plotted are a solid and open circle showing the epicentral location of the best-fit sources using force and moment (solid) and moment-only (open). The lateral extents of the volumes over which our grid search for best-fit source location was performed are shown by bold-solid, light-solid, and dashed squares.

VLP signals at other volcanoes previously in order to probe source processes (Ohminato et al., 1998; Nishimura et al., 2000; Chouet et al., 2003, 2005; Auger et al., 2006; Ohminato et al., 2006; Aster et al., 2008; Chouet et al., 2008; Waite et al., 2008; Chouet et al., 2010; Dawson et al., 2011). Although the waveform inversion method has been described in other publications, we discuss its salient features here for completeness. The waveform inversion method is distinctly different from conventional seismic analysis techniques that rely on the arrival times of seismic phases. Instead of only fitting the arrival times, waveform inversion for the source mechanism seeks to fit the entire seismogram. As a result, the computational demands of waveform inversion far exceed those of standard earthquake location. The main

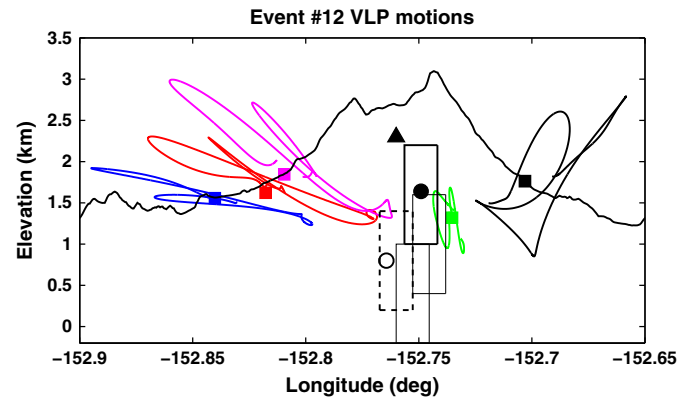


Fig. 7. East–west cross-section of Redoubt at 2 × vertical exaggeration, with the locations of the 5 summit broadband stations projected into the east–west vertical plane. Note that station RD02 (green square) is on the northern flank of the edifice and so appears to be inside of the volcano. The crater is shown as a black triangle and the VLP particle motions show a more or less radial pattern away from a point situated below and to the east of the crater. Also plotted are a solid and open circle showing the locations of the best-fit sources using force and moment (solid) and moment-only (open). The lateral extents of the two volumes over which grid search was performed are shown by bold-solid, light-solid, and dashed rectangles.

advantage of waveform inversion is that it can be applied in principle to any seismic signals, including those at volcanoes that are excited by interactions between gas, liquid, and solid.

Waveform inversion relies on accurate and efficient finite-difference modeling of the seismic wavefield using the method described by Ohminato & Chouet (1997), which includes topography. For Redoubt, we used a 2 arc sec DEM obtained from the USGS seamless server (seamless.usgs.gov) to represent the topography of the volcano. At a nominal latitude of 60°, the DEM has a resolution of approximately 30 m in the east–west direction and 60 m north–south. We interpolate the topography onto a uniform 40 m grid for finite-difference modeling. Whether this resolution meets the requirements for the DEM to accurately represent topography in the finite-difference modeling is determined by considering numerical accuracy. For finite-difference simulations, there should be a certain number of grid points per minimum desired wavelength to ensure accuracy. A rule of thumb based on the finite-difference algorithm of Ohminato & Chouet (1997) states that 25 grid points per wavelength are necessary for accurate modeling. To test this criterion at Redoubt requires that we adopt a subsurface model for the volcano. Based on previous tomography at Redoubt, the P-wave velocity is known to vary from 3.5 km/s at shallow depths to 5 km/s at sea level (Benz et al., 1996; Chouet, 1996). Based on this gross P-wave velocity structure, we take an average P-wave velocity to be 4 km/s. For the other two elastic parameters, S-wave velocity and density, we assume a V_p/V_s ratio of 1.73 to arrive at an S-wave velocity of 2.3 km/s and take the density to be equal to a value typical of the Earth's crust, 2650 kg/m³. Given these model parameters, a grid spacing of 40 m provides accurate finite-difference modeling of S-waves to frequencies as high as 2 Hz, well above our frequency band of interest for VLP signals. In order to avoid ghost edge effects in the finite-difference simulations, we have extended the model 7.6 and 7.2 km away from the crater in the east–west and north–south directions. In addition, the model extends 8 km in depth below the peak of Redoubt, which sits at an elevation of 3.108 km ASL (Chouet et al. 1994). These model dimensions provide a 3D model of Redoubt with 381 × 361 × 201 grid nodes in the east–west, north–south, and vertical directions.

Since elastic wave propagation is a linear problem, any source with a general source time function can be computed provided impulse responses, or Green's functions, are available for all the interior nodes of the model. In finite-difference modeling, a true impulse response can be contaminated by artificial numerical dispersion since the impulse contains high frequencies that do not satisfy the criterion of 25 grid points per wavelength. For this reason, we model approximate impulses to synthesize a general source time function. The approximate impulse is given by (Chouet et al., 2005):

$$S(t) = \begin{cases} \frac{1}{2} \left[1 - \cos\left(\frac{2\pi t}{t_p}\right) \right] & 0 \leq t \leq t_p, \\ 0, & t > t_p, \end{cases} \quad (1)$$

where t is time, $S(t)$ is the elementary source time function, t_p is the characteristic period of this elementary source time function. For our application at Redoubt, we used $t_p = 2$ s.

Now consider that, at a single grid point in the subsurface at Redoubt, we excite seismic sources using the basic source time function given in Eq. (1). At that grid point, we must consider two primary types of seismic sources – a force vector and a symmetric moment tensor. Together, these two types of sources comprise 9 independent components: 3 due to the force and 6 from the symmetric moment tensor. By exciting each of these 9 source components with the basic source time function given in Eq. (1) and saving the Green's functions, the response of any source with a general source time function can be computed with the following matrix–vector equation:

$$\mathbf{d} = \mathbf{G}\mathbf{m} \quad (2)$$

where \mathbf{d} is the data vector, \mathbf{G} is a matrix containing time-shifted Green's functions in each column, and \mathbf{m} is the source mechanism vector. The size of the data vector in Eq. (2) is $N_t N_s \times 1$ where N_t is the number of traces (i.e., data channels) and N_s is the number of time samples. The source mechanism vector is of size $N_m N_b \times 1$ where N_m is the number of possible source types (e.g., 3 forces and 6 moments give $m = 9$) and N_b is the number of elementary functions used to represent the source time functions. This means that matrix \mathbf{G} is a $N_t N_s \times N_m N_b$ matrix.

The procedure for source mechanism inversion consists of solving Eq. (2) for many grid points in the subsurface by least-squares without damping. This requires that Green's functions are known over a volume in the subsurface model. Once the responses at the seismic stations are computed for a source at a particular grid point, errors (in %) between the synthetics and the data are measured according to two definitions given by (Ohminato et al., 1998)

$$E_1 = \frac{\sum_{n=1}^{N_t} \sum_{p=1}^{N_s} (u_n^0(p\Delta t) - u_n^s(p\Delta t))^2}{\sum_{n=1}^{N_t} \sum_{p=1}^{N_s} (u_n^0(p\Delta t))^2} \times 100, \quad (3)$$

and

$$E_2 = \frac{1}{N_r} \sum_{n=1}^{N_t} \frac{\sum_{p=1}^3 \sum_{s=1}^{N_s} (u_n^0(p\Delta t) - u_n^s(p\Delta t))^2}{\sum_{p=1}^3 \sum_{s=1}^{N_s} (u_n^0(p\Delta t))^2} \times 100. \quad (4)$$

where u_n^0 is the data for channel n , u_n^s is the synthetic or modeled data for the n -th channel, and Δt is the sample rate of the seismograms. For a source mechanism given by either 3 forces, 6 moment tensor components, or 3 forces and 6 moments, the grid point with the minimum error corresponds to the optimal source location for that particular mechanism. The two definitions for error in Eqs. (3) and (4) measure the error in different ways. The first definition in Eq. (3) weighs the errors on the data channels with the largest signals most heavily. Since radial motions are typically large for explosive events, E_1 tends to focus on the errors associated with the radial components. In contrast, the second definition in Eq. (4) attempts to normalize the signals between all the components and thus offers a more balanced measure of the errors on all data channels. For this reason we use E_2 to select between different candidate sources that share the same mechanism.

Once the optimal source locations are found for each of the three types of source mechanisms, the best fit among the three different mechanisms can be chosen according to the one that minimizes the Akaike Information Criterion (AIC) (Akaike, 1974)

$$\text{AIC} = N_t N_s \ln E + 2N_m N_b \quad (5)$$

where $N_t N_s$, N_m , and N_b have been described previously and either E_1 or E_2 can be used in place of the error E . The AIC criterion penalizes possible solutions for having both large errors compared to the data and having too many free parameters. The solution that minimizes the AIC criterion in principle captures the optimal tradeoff between error reduction and model complexity. As discussed by Dawson et al. (2011), other types of judgment can be used as well in the final selection, especially when there is limited observational data.

In summary, the procedure for source mechanism inversion is to perform a grid search over the spatial location coordinates while solving Eq. (2) for each possible source location using least-squares. Grid search is the most robust type of inversion procedure because in principle it samples all of the parameter space. Furthermore, the linear inversion of Eq. (2) means that an initial guess for the source mechanism is not needed.

Although the above description of the inversion is valid in principle, three crucial considerations make the procedure drastically more numerically efficient. These considerations involve a) the use of reciprocity to obtain Green's functions over a volume in the subsurface, b) the construction of moment tensor Green's functions from combinations of force Green's functions, and c) the reformulation of Eq. (2) in the frequency domain, as described by Auger et al. (2006) and implemented by Waite et al. (2008) and Chouet et al., (2010). The reciprocity property (Aki & Richards, 1980) involves switching the source and receiver locations and components according to

$$G_{mn}(\mathbf{x}_1, \mathbf{x}_2) = G_{nm}(\mathbf{x}_2, \mathbf{x}_1). \quad (6)$$

This equation states that the m -component of displacement at \mathbf{x}_1 due to a force source applied in the n -direction at \mathbf{x}_2 ($G_{mn}(\mathbf{x}_1, \mathbf{x}_2)$) is equal to the n -component of displacement at \mathbf{x}_2 due to a force source applied in the m -direction at \mathbf{x}_1 ($G_{nm}(\mathbf{x}_2, \mathbf{x}_1)$). The reciprocity property means that receivers can be interchanged for sources in the numerical modeling. This is important since there are typically many more possible source locations than seismic stations. For instance, at Redoubt, there are 13 data channels and we searched for the source location over a subsurface volume of $21 \times 21 \times 31$ grid points. Using reciprocity, only 13 finite-difference modeling runs need to be completed instead of over 40,000. We obtain the estimate of over 40,000 by considering three orthogonal forces individually sourced at each of the $21 \times 21 \times 31$ grid points. Note that the need for disk space to store the Green's functions is not removed by using reciprocity. Additional computational savings are obtained by only modeling Green's functions using force sources. The moment tensor Green's functions are then formed from the different force components.

The final gain in numerical efficiency is achieved by using the frequency domain version of Eq. (2). The efficiency in this case arises from the fact that the finite-difference model is time invariant. Eq. (2), being in the time domain, could hypothetically accommodate a Green's function for a medium whose properties changed with time. Note that we are specifically discussing medium properties that change over the short time scale it takes for waves to propagate from the volcanic source to the receivers. Since the subsurface model at Redoubt is taken to be constant with time, the ability to accommodate time-changing material properties is not needed. Thus, it makes sense to take a Fourier transform over time since the matrix \mathbf{G} is time invariant. In the frequency domain, many smaller matrices are inverted as opposed to one single large matrix in the time domain. Note that, when working in the frequency domain, the parameter N_b is replaced by the number of frequencies N_f and the AIC criterion becomes

$$\text{AIC} = N_t N_s \ln E + 2N_m N_f. \quad (7)$$

5. Results

We conducted grid searches for the optimal source composed of 3 forces, 6 moments, and 3 forces and 6 moments within four volumes at Redoubt. The four volumes are shown as bold-solid, light-solid, and dashed boxes in Figs. 6 and 7. Each volume consisted of $21 \times 21 \times 31$ gridpoints in the east–west, north–south, and vertical directions. The four volumes overlapped in some regions of the subsurface. The results of the 3 types of source mechanism inversions are summarized in Table 1. Although source time functions are computed over a full time window of 204.75 s, the errors are only computed from 10 to 195 s. From the error and AIC reduction, a source at Redoubt that is based on a single force can be ruled out immediately. The locations of the optimal sources based on force and moment and moment-only are also shown in Figs. 6 and 7. The force and moment and moment-only solutions are located in the bold-solid and dashed

boxes in Figs. 6 and 7, respectively. A distinct difference in the locations exists in the vertical direction, as seen in Fig. 7, with the solution based on force and moment being shallower (1.6 km ASL) than the moment-only solution (0.8 km ASL). Even when considering a volume of source locations within 1% of the minimum error, the error volumes for the two mechanisms do not overlap. The two solutions are also in different lateral locations as shown in Fig. 6. The force and moment solution sits to the northeast of the crater whereas the moment-only solution lies to the southwest.

Simply based on considering AIC reduction in Table 1, the force and moment solution would be chosen as the best-fitting mechanism. The excellent fit of the force and moment solution can be observed in Fig. 8, which shows the waveform match between the data and finite-difference modeling. All waveforms are well-matched, except for possibly the vertical component of RDWB. By comparison, the fit between the moment-only solution and the data in Fig. 9 is noticeably worse, although still overall capable of matching the largest signals. Based on the AIC, the improved data-fitting in Fig. 8 is apparently worth the cost of introducing 3 new model parameters. In the next section, we discuss the merits of the force and moment solution in light of the limited amount of data (13 channels) at Redoubt. The situation is similar to that encountered at Augustine Volcano (Dawson et al., 2011), where only 14 data channels were available. Finally, note the strong similarity between the east–west components of RD03, RDWB, and RDW in either Fig. 8 or Fig. 9. We point this out in light of the earlier discussion on the switching of the horizontal components for station RDWB. Had this switching not been taken into account, the large east–west component for RDWB would have instead been associated with the north–south component, as seen in the raw data. Due to the proximity of RD03, RDWB, and RDW, we believe the switching of the horizontal components for RDWB makes sense, although we are unable to identify the specific cause of the switch.

Fig. 10 shows the source time functions for the force and moment solution. The waveforms for the individual moments are consistently shaped and are dominated by the volumetric opponents along the main diagonal. In addition, the M_{zz} component dominates over the two horizontal components M_{xx} and M_{yy} . The average amplitude ratios of the force components to the moment components, F_x/M_{xx} , F_y/M_{yy} , and F_z/M_{zz} , are approximately $8 \times 10^{-5} \text{ m}^{-1}$, suggesting that the single force contributed less than 10% to the waveforms (Dawson et al., 2011). The inverted source time functions for the moment-only solution (Fig. 11) shows similar characteristics consistent with those seen for the moments in Fig. 10. The moment tensor is again observed to be dominated by the diagonal components, indicating a volumetric source with M_{zz} as dominant component. However, notice that the amplitude of the M_{zz} component of the moment tensor is 4 times smaller in the moment-only solution, which has a peak-to-peak amplitude of $\sim 6.5 \times 10^{14} \text{ Nm}$ instead of $\sim 25 \times 10^{14} \text{ Nm}$ in the force and moment solution in Fig. 10. In the next section, we discuss this discrepancy when judging which of the two solutions is ultimately the most robust and reliable at Redoubt.

Since the location of the best-fit source is found through grid search, the uncertainties in source location can be visualized by plotting the error in the volume within the finite-difference model over which the search was completed. This error volume for E_2 is plotted for the force and moment solution in Fig. 12. It is clear that the source location is better constrained in the east–west direction than the north–

Table 1
Residual errors for free inversions and corresponding AIC.

Source mechanism	Error $E_1\%$	Error $E_2\%$	AIC(E_1)	AIC(E_2)
Force only	70.8	105.6	–6099	15,189
Moment only	7.1	14.2	–116,270	–79,360
Moment and force	3.6	3.8	–140,140	–137,270

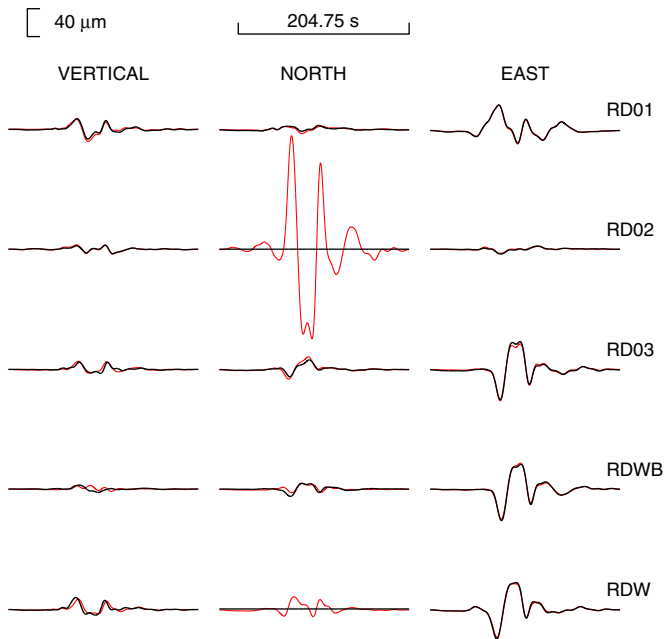


Fig. 8. Waveform fits from the source mechanism inversion for 6 moments and 3 forces. The three columns are, from the left to right, the vertical, north–south, and east–west components, respectively. Each row corresponds to one of the five summit broadband, ordered from top to bottom as RD01, RD02, RD03, RDWB, and RDW.

south direction. This makes sense because the 5 stations have better coverage in the east–west direction than north–south. In fact, the resolution in the north–south direction is controlled greatly by a single station, RD02. The greatest tradeoff in the location appears to be in

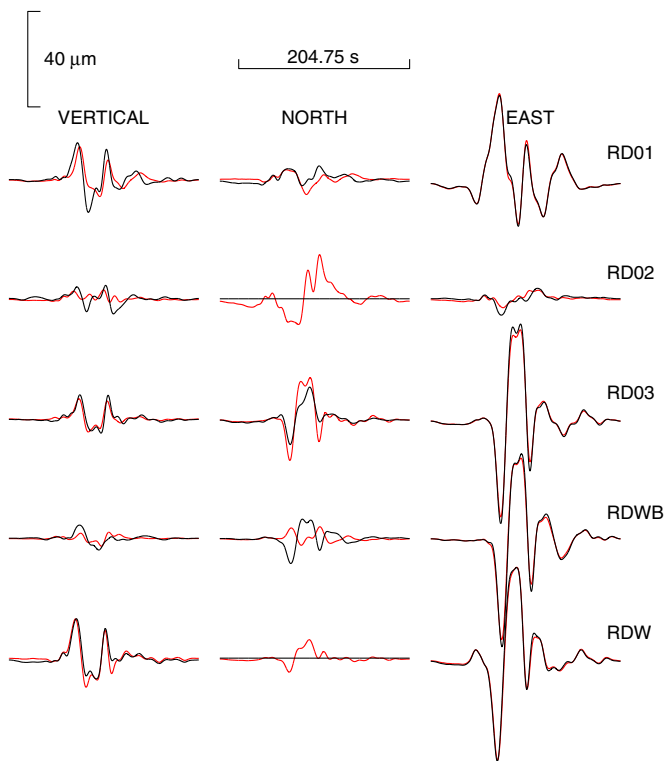


Fig. 9. Waveform fits from the source mechanism inversion for 6 moments only. The three columns are, from the left to right, the vertical, north–south, and east–west components, respectively. Each row corresponds to one of the five summit broadband, ordered from top to bottom as RD01, RD02, RD03, RDWB, and RDW.

the north–south plane, where the location can become deeper and farther south without strongly changing the residual error.

The poorer resolution in the north–south direction also has an effect on the distribution of the point-by-point eigenvectors for the moment tensor from the force and moment solution. We show this effect in Fig. 13, where we have computed the eigenvectors for the inverted moment tensor for the force and moment solution. We view the eigenvectors from both the south (left panel) and the east (right panel). The eigenvectors are computed for each point within the inverted moment tensors when the amplitudes exceed 30% of the peak value (Waite et al., 2008). The eigenvectors for both solutions show much more stability in the east–west direction, which is apparent in the left panel when the view is from the south. The eigenvectors are less stable in the north–south direction, as evidenced by the spread in the distribution of vectors in the right panel. Although we show this property in Fig. 13 for the moment tensor from the force and moment solution, we note that the same property is observed for the moment tensor from the moment-only solution. In both cases, the dominant dipole of the inverted moment tensors is in the vertical direction.

6. Discussion

The inverted moment tensors for the both the force and moment solution and the moment-only solution share some interesting common characteristics. However, in this section we point out that there are significant differences between the two solutions that cast doubt on the reliability of the force and moment solution. Ultimately, we prefer the moment-only solution in spite of the poorer data fit given in Table 1. We attribute the improved fit of the force and moment solution to the limited number of data channels at Redoubt, similar to the situation at Augustine where limited observational data were available (Dawson et al., 2011). These issues of receiver coverage are important as volcanoes are inherently difficult places to deploy broadband instruments and data-limited situations are often encountered in practice.

From measurements of peak-to-peak amplitudes, the eigenvector ratios for the force and moment solution and the moment-only solution are [0.39:0.75:2.00] and [0.54:0.81:2.00], respectively. For these eigenvector ratios, the largest component (vertical component) has been set to a value of 2 for normalization. These values fall within the statistical bounds for possible moment tensors at Augustine, which were given by Dawson et al. (2011) as $[0.49 \pm 0.22:0.75 \pm 0.14:2.00]$. The time-histories of the moment tensors for the two solutions shown in Figs. 10 and 11 also show a similar pattern of inflation followed by two cycles of deflation–re-inflation. This pattern is seen in the M_{zz} component as upward motion followed by two or more cycles of downward–upward motion. These patterns are consistent with a pressurization (inflation) and depressurization (deflation) of a sill over a time scale of 1–2 min. Note that there may be deflation signals with periods greater than 30 s that we do not measure due to the limitation imposed by the passband of the seismometers. The presence of such signals would mean that the inflation–deflation process we describe could be relatively smaller oscillations superimposed on an overall gradually changing deflation signal. This type of time-history of the moment tensor has been observed previously at Popocatepetl and Augustine volcanoes during explosions (Chouet et al., 2005; Dawson et al., 2011). These common observations point to a general source process for Vulcanian explosions at dome-building volcanoes. A model based on diffusive bubble growth has been proposed to explain this behavior (Nishimura, 2004; Chouet et al., 2006) and has been demonstrated to provide an excellent fit the moment tensor waveform at Popocatepetl (Chouet et al., 2006; Chouet, 2009). The process involves the response of a supersaturated magma to a rapid pressure drop due to explosive degassing. Bubble growth caused by diffusion of volatiles in the supersaturated magma induces the expansion of the source volume, which in turn repressurizes the system.

Although the moment tensors for both the force and moment and moment-only solutions share these common features, they differ greatly

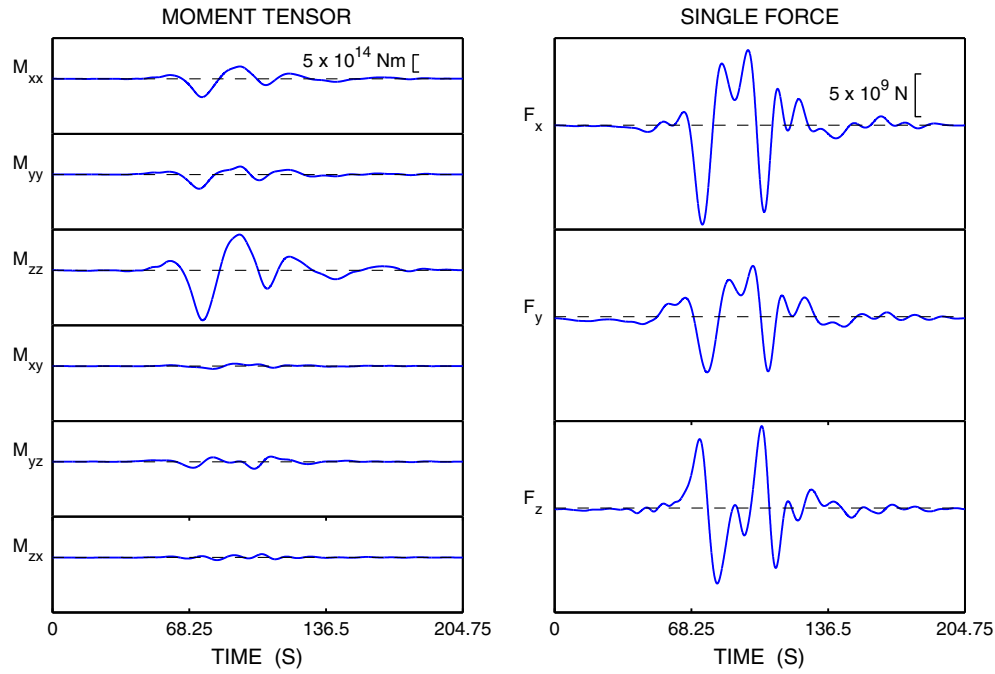


Fig. 10. The source time functions from the source mechanism inversion for 6 moments and 3 forces. From top to bottom, the 6 moments are sorted as M_{xx} , M_{yy} , M_{zz} , M_{xy} , M_{yz} , and M_{zx} . The force components are sorted from top to bottom as F_x , F_y , and F_z . Vertical axes are in SI units, either Nm for moment components or N for the forces.

in both their location and amplitude. From peak-to-peak measurements, the M_{zz} component for the force and moment solution is $\sim 25 \times 10^{14}$ Nm versus a value of $\sim 6.5 \times 10^{14}$ Nm for the moment-only case. The amplitude for the moment-only case provides better agreement with the M_{zz} component of the moment tensor obtained at Augustine, which was on the order of $\sim 4 \times 10^{14}$ Nm. Based on this comparison, it appears

the force and moment solution, on the basis of its additional free parameters, it able to artificially increase the amplitude of the moment tensor while modifying the force vector in a way that still provides a good data fit.

A suspicious property of the force and moment solution is its location, specifically its depth at elevation 1.6 km ASL. This elevation coincides with the average elevation of the 5 broadband stations (1.62 km). Although such a location cannot be ruled out a priori, the fact that the force and moment solution is able to attain a distinct minimum in the residual error at an elevation of 1.6 km, as seen in Fig. 12, evokes some doubt regarding whether it is a reliable solution. Moreover, the particle motions depicted in Figs. 4 and 7 have initial upward motions, which would not be expected for an explosive source located at a higher elevation than some of the stations. Another suspicious coincidence in the force and moment solution is that the lateral component of the force vector in Fig. 10 points in a direction of approximately 70° clockwise from north. This is also the same lateral direction for all the particle motions shown in Fig. 6. Lastly, a compelling piece of evidence against the force and moment solution is that the horizontal components of the force vector in Fig. 10 are not in phase with the vertical component. The lack of a consistent shape among the different force components argues against the existence of such a force. This property of the force vector is in contrast to the moment tensor, whose components are consistently shaped. Unfortunately, the critical absence of the north component of station RD02 precludes any strong constraint on our solution in that direction. It is clear from Figs. 8 and 9 that the north component of station RD02, were it available, would provide a strong test between the force and moment and moment-only solutions. Based on these coincidences in the force and moment solution, and the conclusions from (Dawson et al., 2011) regarding the resolution of limited broadband networks, we prefer the moment-only solution occurring at a depth of 0.8 km ASL, in spite of its reduced data fit.

From the principal axes of the moment-only solution, we can estimate the volume and pressure changes at the VLP source. To do so, we first find the projection of the principal axes [0.54:0.81:2.00], onto the principal axes of the moment tensors for three orthogonal cracks given by the ratios [2:1:1], [1:2:1], and [1:1:2]. These represent cracks set in planes normal to the x-, y-, and z-directions, respectively, in the coordinate frame defined by the principal axes. The principal axes

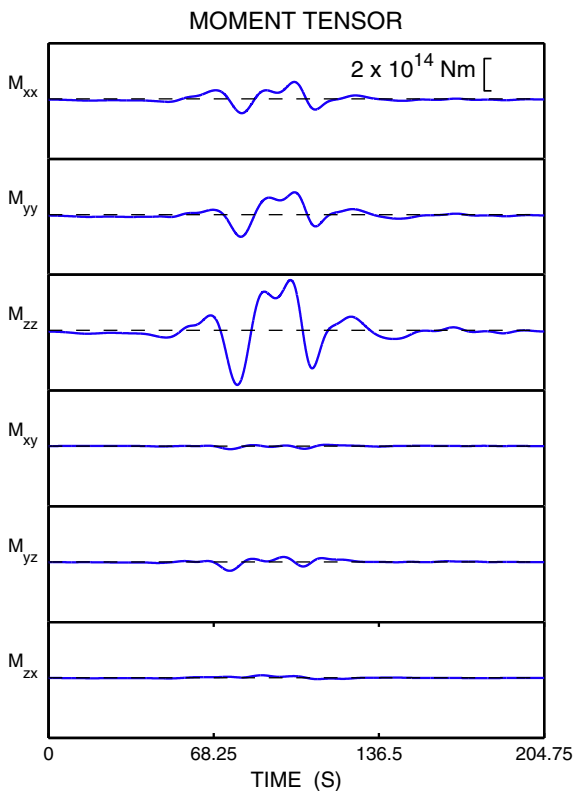


Fig. 11. The source time functions from the source mechanism inversion for 6 moments only. From top to bottom, the 6 moments are sorted as M_{xx} , M_{yy} , M_{zz} , M_{xy} , M_{yz} , and M_{zx} . Vertical axes are in SI units of Nm for moment components.

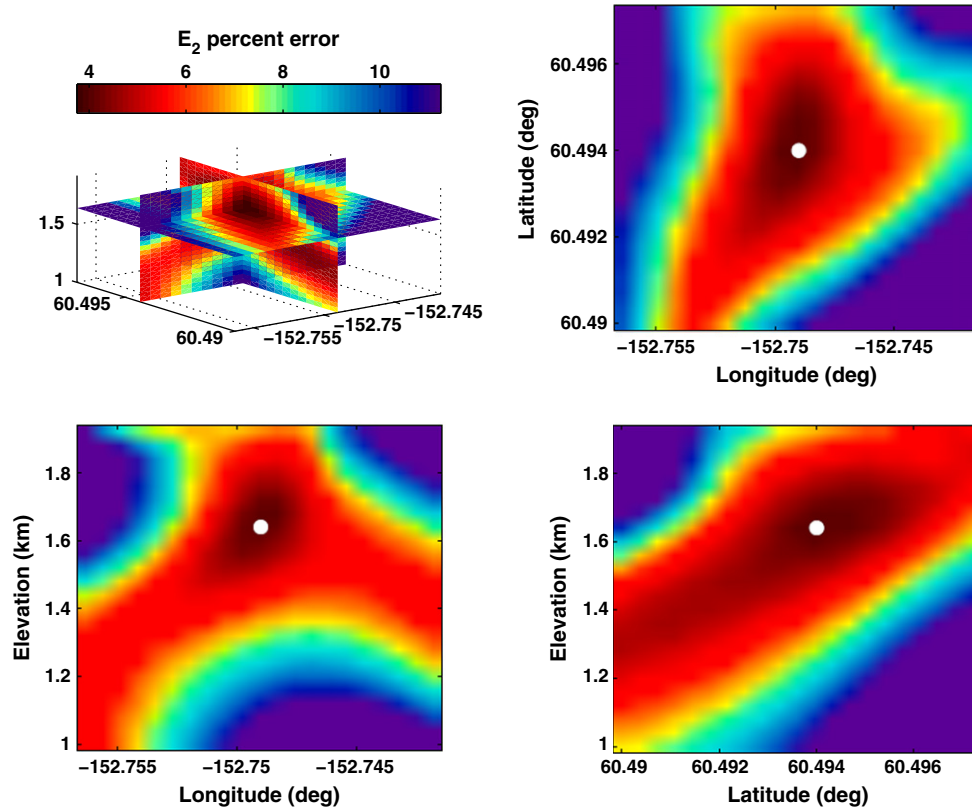


Fig. 12. Slices from the error volume for the inversion for 6 moments and 3 forces. The minimum error solution is shown as a white circle. The slices are through the error volume outlined by the solid square and rectangle in Figs. 6 and 7.

estimated from the source time functions that we use here are normalized to have a maximum component equal to 2. The actual principal axes we estimate are equal to $[0.54:0.81:2.00] \times 3.3 \times 10^{14}$ Nm. The principal axes of the moment tensor for a tensile crack have amplitudes $\lambda\Delta V$, $\lambda\Delta V$, and $(\lambda + 2\mu)\Delta V$, where ΔV is the volume change

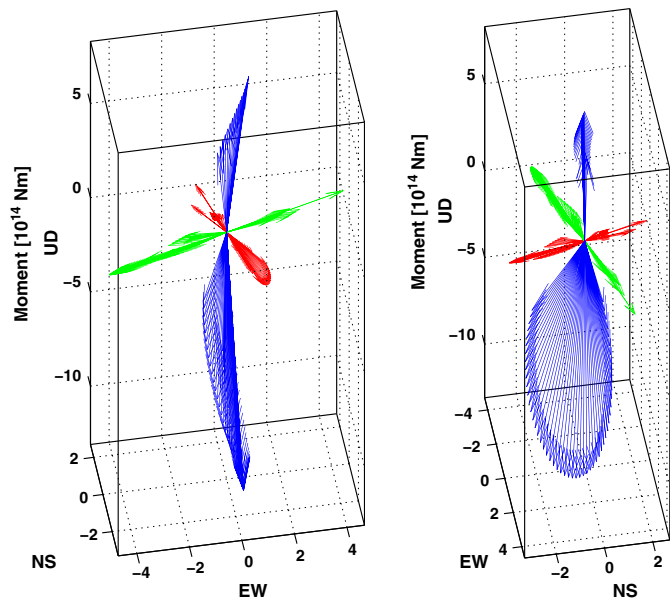


Fig. 13. (Left panel) Moment tensor eigenvectors viewed from the south for the force and moment solution. (Right panel) The same eigenvectors as in the left panel, except viewed from the east. The color scheme in the panels is as follows: major eigenvector (blue), intermediate eigenvector (green), and minor eigenvector (red).

due to the crack opening or closing, λ is Lamé's first coefficient of the rock matrix, and μ is the shear modulus (Chouet et al., 2005). As a result, the above ratios for the cracks assume a Poisson ratio of 1/3 at the source ($\lambda = 2\mu$), a value appropriate for volcanic rock at or near liquidus temperatures (Murase & McBirney, 1973; Chouet, 1996). The principal axes in this case are equal to $2\mu\Delta V [1:1:2]$, for example. To find the projection onto the 3 orthogonal cracks, we solve the matrix equation

$$\begin{bmatrix} 0.54 \\ 0.81 \\ 2.00 \end{bmatrix} = \begin{bmatrix} 2 & 1 & 1 \\ 1 & 2 & 1 \\ 1 & 1 & 2 \end{bmatrix} \begin{bmatrix} C_x \\ C_y \\ C_z \end{bmatrix} \quad (8)$$

for the coefficients of the 3 cracks, C_x , C_y , and C_z . The solution gives $C_x = -0.30$, $C_y = -0.03$, and $C_z = 1.16$. From these ratios, the crack normal to the y-direction contributes little compared to the other cracks and can be ignored. The ratio of the other two cracks gives $C_x/C_z = -0.26$. By combining two cracks in this ratio, we obtain

$$\frac{2}{2-0.26} \times ([1:1:2] - 0.26 \times [2:1:1]) = [0.55:0.85:2.00], \quad (9)$$

which is close to the principal axes derived from the source time function, $[0.54:0.81:2.00]$. This decomposition suggests that a dominant sill and a subdominant dike exist at the source location, with the dike contributing 26% of the volume change of the sill. Since the sill and dike are combined with a ratio equal to -0.26 , the sill and dike are out of phase with one inflating while the other is deflating. Recall that the principal axes derived from the source time function include the multiplier 3.3×10^{14} Nm. This multiplier is equal to the product $2\mu\Delta V \times (2 - 0.26)/2$, where ΔV is the volume change in the sill. By assuming $\mu = 10$ GPa (Chouet et al., 2005), this gives a volume change in the sill of $19,000 \text{ m}^3$. As discussed by Chouet et al., (2005), the volume change in the sill can be related to the associated pressure

change according to $\Delta P = (9\mu/16)(\Delta V/R^3)$, where R is the radius of the sill. If we take $R = 250$ m as a characteristic length scale for the sill, the pressure change is equal to 7 MPa. For the subdominant dike, we similarly compute $\Delta V = 5000\text{m}^3$ and $\Delta P = 1.8$ MPa. The dominant sill and subdominant dike are oriented such that the normal vector to the sill is in the z-direction and the normal vector to the dike is in the x-direction within the coordinate frame defined by the principal axes of the moment tensor.

To gain a clearer picture of the geometry of the sill and dike, we need to describe the orientations of the principal axes computed from the moment tensor in geographical coordinates. We find that the normal vector to the sill has an azimuth of $\phi = 80^\circ$ and forms an angle of $\theta = 77^\circ$ with the horizontal plane. Note that our convention for the ϕ and θ angles follows Chouet et al. (2005): azimuth ϕ is degrees counterclockwise from east and elevation angle θ is degrees above the horizontal plane. Given these conventions, the dominant sill is subhorizontal and tilted slightly to the NE. In addition to the sill, the normal vector for the dike has an azimuth of $\phi = 112^\circ$ and an elevation angle of $\theta = -10^\circ$. Thus, the dike strikes in the WSW–ENE direction.

Finally, it is interesting to compare the depth we find for the VLP source to the depth of the source of the 23-hour-long precursory swarm of LP events during the 1989–90 Redoubt eruption. Based on careful analysis of the repetitive earthquakes, Lahr et al. (1994) argued that the entire swarm likely originated from a single point 1.4 km below the crater floor, which corresponds to an elevation of approximately 0.9 km ASL. We find the VLP source from the 2009 eruption is at an elevation of 0.8 km ASL, at an almost identical depth to the 1989 LP source. Moreover, the lateral location of the 1989 LP source (Lahr et al., 1994) virtually overlaps with the location we find for the VLP signal from the 2009 eruption. Our interpretation of this consistency in the 2009 VLP and 1989 LP locations is that the VLP source is composed of a dominant sill that acts as a shallow magma storage reservoir, while the 1989 LP source may have involved a crack-like conduit connecting the sill to the shallower magmatic and hydrothermal system at Redoubt. We interpret the common VLP/LP location to be a long-lived feature that sits at the base of the volcanic edifice, at the contact of the volcanic pile with the batholith beneath Redoubt. Thus, both the 1989 LP source and the 2009 VLP source sit at an important structural location in the subsurface. The differences in the precursory seismicity from the 1989 and 2009 eruptions may be the result of variability in the conduit above the VLP/LP location. This point is consistent with the results of Benz et al. (1996), who showed that earthquake locations from the 1989 sequence cluster above the location of the 1989 LP source. We hold off on more quantitative interpretations of the VLP source until complete source reconstructions can be performed using forward modeling of waveforms with composite source with crack and/or pipe components (Chouet et al., 2005, 2008, 2010; Dawson et al., 2011).

7. Conclusion

We have analyzed VLP signals from an explosion at Redoubt Volcano during the 2009 eruption and find a preferred model for the event based on a moment tensor source acting to the southwest of the crater at a depth of 0.8 km ASL. The limited network of broadband seismometers at Redoubt posed a challenge for the interpretation of the solutions based on force and moment versus moment-only. The time-history of the moment tensor from the preferred source model shows a pattern of pressurization and depressurization that agrees with previous studies of VLP signals associated with explosions at Popocatepetl and Augustine volcanoes. Open questions about the VLP signals at Redoubt remain concerning which reconstructed source model provides the best fit to the data. In addition, the relation between the excitations of the VLP signals and the 2009 LP swarms is an interesting challenge for future work. Finally, the inversion of other explosive events during the 2009 Redoubt eruption should shed light on the evolution of the magmatic system during the early

stages of the eruption, from March 23 until the final dome-destroying explosion on April 4. We have demonstrated how to proceed with the interpretation of source mechanism inversions in the presence of limited broadband seismic data and have shown that the methodology can still provide valuable characterization of VLP source processes.

Acknowledgments

This work has benefited from the comments of 3 anonymous reviewers. We thank Helena Buurman and Cyrus Read from AVO for bravely deploying the temporary broadbands at Redoubt in the days before the explosive phase of the eruption began. The computational modeling for this study was performed on the Sonic cluster at Boise State University.

References

- Akaike, H., 1974. A new look at the statistical model identification. *IEEE Transactions on Automatic Control* 19, 716–723.
- Aki, K., Richards, P., 1980. *Quantitative Seismology*. W. H. Freeman and Company, San Francisco.
- Almendros, J., Chouet, B., 2003. Performance of the radial semblance method for the location of very long period volcanic signals. *Bulletin of the Seismological Society of America* 93, 1890–1903.
- Arciniega-Ceballos, A., Chouet, B.A., Dawson, P., 1999. Very long-period signals associated with Vulcanian explosions at Popocatepetl, Volcano, Mexico. *Geophysical Research Letters* 26, 3013–3016.
- Arciniega-Ceballos, A., Chouet, B., Dawson, P., Asch, G., 2008. Broadband seismic measurements of degassing activity associated with lava effusion at Popocatepetl, Volcano, Mexico. *Journal of Volcanology and Geothermal Research* 170, 12–23.
- Aster, R., Zandomenighi, D., Mah, S., McNamara, S., Henderson, D.B., Knox, H., Jones, K., 2008. Moment tensor inversion of very long period seismic signals from Stromboli eruptions of Erebus Volcano. *Journal of Volcanology and Geothermal Research* 177, 635–647.
- Auger, E., D'Auria, L., Martini, M., Chouet, B., Dawson, P., 2006. Real-time monitoring and massive inversion of source parameters of very long period seismic signals: an application to Stromboli Volcano, Italy. *Geophysical Research Letters* 33, L04301.
- Benz, H.M., Chouet, B.A., Dawson, P.B., Lahr, J.C., Page, R.A., Hole, J.A., 1996. Three-dimensional P and S wave velocity structure of Redoubt Volcano, Alaska. *Journal of Geophysical Research* 101, 8111–8128.
- Cesca, S., Battaglia, J., Dahm, T., Tessmer, E., Heimann, S., Okubo, P., 2008. Effects of topography and crustal heterogeneities on the source estimation of LP event at Kilauea volcano. *Geophysical Journal International* 172, 1219–1236.
- Chouet, B., 1996. New methods and future trends in seismological volcano monitoring. In: Scarpa, R., Tilling, R.I. (Eds.), *Monitoring and Mitigation of Volcano Hazards*. Springer, New York, pp. 23–97.
- Chouet, B., 2009. Nonlinear processes in volcanoes. In: Meyers, R.A. (Ed.), *Encyclopedia of Complexity and Systems Science*, volume 10. Springer, New York, pp. 9872–9899.
- Chouet, B.A., Page, R.A., Stephens, C.D., Lahr, J.C., Power, J.A., 1994. Precursory swarms of long-period events at Redoubt Volcano (1989–1990), Alaska: their origin and use as a forecasting tool. *Journal of Volcanology and Geothermal Research* 62, 95–135.
- Chouet, B., Dawson, P., Ohminato, T., Martini, M., Saccorotti, G., Giudicepietro, F., Luca, G.D., Milana, G., Scarpa, R., 2003. Source mechanisms of explosions at Stromboli Volcano, Italy, determined from moment-tensor inversions of very-long-period data. *Journal of Geophysical Research* 108, 2019.
- Chouet, B., Dawson, P., Arciniega-Ceballos, A., 2005. Source mechanism of Vulcanian degassing at Popocatepetl Volcano, Mexico, determined from waveform inversion of very long period signals. *Journal of Geophysical Research* 110, B07301.
- Chouet, B., Dawson, P., Nakano, M., 2006. Dynamics of diffusive bubble growth and pressure recovery in a bubbly rhyolitic melt embedded in an elastic solid. *Journal of Geophysical Research* 111, B07310.
- Chouet, B., Dawson, P., Martini, M., 2008. Shallow-conduit dynamics at Stromboli Volcano, Italy, imaged from waveform inversions. In: Lane, S.J., Gilbert, J.S. (Eds.), *Fluid Motions in Volcanic Conduits: A Source of Seismic and Acoustic Signals*. Geological Society of London, London, pp. 57–84.
- Chouet, B.A., Dawson, P.B., James, M.R., Lane, S.J., 2010. Seismic source mechanism of degassing bursts at Kilauea Volcano, Hawaii: results from waveform inversion in the 10–50 s band. *Journal of Geophysical Research* 115, B09311.
- Dawson, P.B., Benitez, M.C., Chouet, B.A., Wilson, D., Okubo, P.G., 2010. Monitoring very-long-period seismicity at Kilauea Volcano, Hawaii. *Geophysical Research Letters* 37, L18306.
- Dawson, P.B., Chouet, B.A., Power, J., 2011. Determining the seismic source mechanism and location for an explosive eruption with limited observational data: Augustine Volcano, Alaska. *Geophysical Research Letters* 38, L03302.
- DeLauro, E., DeMartino, S., Falanga, M., Palo, M., Scarpa, R., 2005. Evidence of VLP volcanic tremor in the band [0.2–0.5] Hz at Stromboli volcano, Italy. *Geophysical Research Letters* 32, L17303.

- Fee, D., McNutt, S., Arnoult, K., Szuberla, C., Olson, J., Lopez, T., 2013. Combining local and remote infrasound recordings from the 2009 Redoubt Volcano Eruption. *Journal of Volcanology and Geothermal Research* 259, 100–114.
- Haney, M.M., 2010. Location and mechanism of very long period tremor during the 2008 eruption of Okmok Volcano from interstation arrival times. *Journal of Geophysical Research* 115, B00B05.
- Haney, M.M., Power, J., West, M., Michaels, P., in press. Causal instrument corrections for short-period and broadband seismometers. *Seismological Research Letters*.
- Hotovec, A., Prejean, S., Vidale, J., Gombert, J., 2013. Strongly gliding harmonic tremor during the 2009 Eruption of Redoubt Volcano. *Journal of Volcanology and Geothermal Research* 259, 89–99.
- Kumagai, H., Ohminato, T., Nakano, M., Ooi, M., Kubo, A., Inoue, H., Oikawa, J., 2001. Very-long-period seismic signals and Caldera Formation at Miyake Island, Japan. *Science* 293, 687–690.
- Lahr, J.C., Chouet, B.A., Stephens, C.D., Power, J.A., Page, R.A., 1994. Earthquake classification, location, and error analysis in a volcanic environment: implications for the magmatic system of 1989–90 eruptions of Redoubt Volcano, Alaska. *Journal of Volcanology and Geothermal Research* 62, 137–151.
- Lyons, J.J., Waite, G.P., 2011. Dynamics of explosive volcanism at Fuego volcano imaged with very long period seismicity. *Journal of Geophysical Research* 116, B09303.
- Murase, T., McBirney, A.R., 1973. Properties of some common igneous rocks and their melts at high temperatures. *Geological Society of America Bulletin* 84, 3563–3592.
- Nishimura, T., 2004. Pressure recovery in magma due to bubble growth. *Geophysical Research Letters* 31, L12613.
- Nishimura, T., Kobayashi, T., Ohtake, M., Sato, H., Nakamichi, H., Tanaka, S., Sato, M., Ueki, S., Hamaguchi, H., 2000. Source processes of very long period seismic events associated with the 1998 activity of Iwate Volcano, northeastern Japan. *Journal of Geophysical Research* 105, 19135–19147.
- Ohminato, T., Chouet, B.A., 1997. A free-surface boundary condition for including 3D topography in the finite-difference method. *Bulletin of the Seismological Society of America* 87, 494–515.
- Ohminato, T., Chouet, B.A., Dawson, P., Kedar, S., 1998. Waveform inversion of very long period impulsive signals associated with magmatic injection beneath Kiluaea Volcano, Hawaii. *Journal of Geophysical Research* 103, 23,869–23,862.
- Ohminato, T., Takeo, M., Kumagai, H., Yamashina, T., Oikawa, J., Koyama, E., Tsuji, H., Urabe, T., 2006. Vulcanian eruptions with dominant single force components observed during the Asama 2004 volcanic activity in Japan. *Earth Planets Space* 58, 583–593.
- Power, J.A., Lahr, J.C., Page, R.A., Chouet, B.A., Stephens, C.D., Harlow, D.H., Murray, T.L., Davies, J.N., 1994. Seismic evolution of the 1989–1990 eruption sequence of Redoubt Volcano, Alaska. *Journal of Volcanology and Geothermal Research* 62, 69–94.
- Power, J.A., Stihler, S.D., Chouet, B.A., Haney, M.M., Ketner, D.M., 2013. Seismic observations of Redoubt Volcano, Alaska — 1989–2010 and a conceptual model of the Redoubt magmatic system. *Journal of Volcanology and Geothermal Research* 259, 31–44.
- Waite, G.P., Chouet, B.A., Dawson, P.B., 2008. Eruption dynamics at Mount St. Helens imaged from broadband seismic waveforms: interaction of the shallow magmatic and hydrothermal systems. *Journal of Geophysical Research* 113, B02305.